J. Fluid Mech. (2012), *vol.* 706, *pp.* 470–495.
doi:10.1017/jfm.2012.269

Control of the secondary cross-flow instability using localized suction

Tillmann Friederich and Markus J. Kloker†

Institut für Aerodynamik und Gasdynamik, Universität Stuttgart, Pfaffenwaldring 21, D-70550 Stuttgart, Germany

(Received 4 October 2011; revised 16 March 2012; accepted 4 June 2012; first published online 13 July 2012)

Transition control by suction in a three-dimensional boundary-layer flow subject to cross-flow instability is investigated using direct numerical simulation. Whereas the classical application of (homogeneous) suction at the wall is aimed at modifying the quasi-two-dimensional base flow to weaken primary cross-flow instability, here the three-dimensional nonlinear disturbance state with large-amplitude steady cross-flow vortices (CFVs) is controlled. Strong, localized 'pinpoint' suction is shown to be suitable for altering the CFVs and the associated flow field such that secondary instability is weakened or even completely suppressed. Thus significant delay of transition to turbulence can be achieved.

Key words: drag reduction, instability control, transition to turbulence

1. Introduction

Improving the fuel efficiency of aircraft has become an important task. Not only do airlines benefit from decreasing their direct operational costs by saving increasingly expensive fuel, but also the environmental aspect has gained growing interest, and regulators are presently looking at limiting greenhouse gas emissions.

To date, the actual optimizations applied to new airplanes have been limited to enhanced shaping, higher surface quality and engine improvement, and it is thought that there is little potential left in these research fields. New concepts have therefore to be envisaged. Laminar flow control (LFC) provides a total drag reduction potential of up to 16 % by, for example, realizing 40 % laminar flow on wings and tail planes of a current airliner (Schrauf 2005).

Intense research on LFC has been carried out within the past few decades. For plane boundary-layer flows without cross-flow, (homogeneous) suction at the wall has been shown to delay transition to turbulence significantly by pulling high-momentum fluid towards the wall, thus enforcing fuller wall-normal profiles of the streamwise velocity which lead to attenuated growth of Tollmien–Schlichting (TS) instability waves. Also, active TS wave control, by triggering antiphase disturbances, now allows successful control of an unstable two-dimensional boundary layer.

As for three-dimensional boundary layers with favourable (negative) streamwise pressure gradient, suction is employed for a reduction of the basic cross-flow: primary cross-flow instability leads to growth of steady and travelling cross-flow vortices (CFVs). Owing to surface roughness, steady CFVs typically prevail and cause early transition on a swept airliner wing if the sweep angle is larger than $\sim 25^\circ$. Several

† Email address for correspondence: kloker@iag.uni-stuttgart.de

flight campaigns were conducted in the USA and Europe starting in the early 1960s. Based on the overviews by Joslin (1998*a*,*b*), the most important issues have been summarized in the direct numerical simulation (DNS) work by Messing & Kloker (2010). Among others, the Northrop X-21 flight tests, the NASA Jetstar campaign, the Boeing 757 HLFC test and the Airbus A320 fin test showed reportedly successful transition delay and significant extensions of laminar flow regions. Slit suction systems (X-21) as well as suction-hole panels were employed. However, the physics of the laminar–turbulent breakdown of boundary layers with cross-flow had not been fully understood at that time. Only later, after fundamental research, the complete cross-flow transition process was fully elucidated including the secondary instability of CFVs by means of experiments (see e.g. Bippes 1999; Saric, Reed & White 2003; White & Saric 2005), theory (see Malik *et al.* 1999; Koch *et al.* 2000) and DNSs (see Wassermann & Kloker 2002, 2003, 2005).

Several other methods aiming at control of cross-flow transition have been developed meanwhile. Saric, Carrillo & Reibert (1998*a*,*b*) proposed the distributed roughness elements (DRE) technique – for a recent overview, see Saric, Carpenter & Reed (2008). A one-time excitation of steady CFVs that are spaced more narrowly in the spanwise direction than the naturally most amplified ones enforces a flow scenario with, at first, secondarily stable CFVs and thus delays transition to turbulence. The upstream flow deformation concept (UFD), proposed by Wassermann & Kloker (2002), pursues a similar goal, not necessarily based on roughness.

Kloker (2008) and also Messing & Kloker (2010) proposed a combination of UFD and suction leading to the concept of distributed flow deformation (DFD) and in particular formative suction. A slot-suction panel can be designed such that narrowly spaced useful vortices are continuously excited and maintained, enhancing the effect of bare suction. Also, successive panels can be adapted to the altering stability characteristics of the base flow when proceeding downstream and thus continuously excite the locally optimal DFD mode.

To date, (homogeneous) suction for LFC has mostly been applied to alter the base-flow stability characteristics in order to attenuate the growth of primary-instability disturbances in the linear disturbance state. It was believed that, once the flow is dominated by large-amplitude, secondarily unstable CFVs, it is no longer amenable to effective control.

The idea of directly influencing the nonlinear disturbance state with developed CFVs in the stage of already active secondary instabilities arose from the finding that even a small velocity component normal to a local shear layer can substantially reduce the shear-layer instability (see Bonfigli & Kloker 2007; Friederich & Kloker 2008; Kloker 2008). Localized, strong suction through holes at the wall at the updraft side of the cross-flow vortex, i.e. the position of the eigenfunction maximum of the most amplified high-frequency secondary modes, may reduce their growth while also hampering the vortical motion.

The aim of this paper is to investigate the novel concept to control the secondary instability of three-dimensional boundary layers by means of localized suction. The underlying base flow corresponds to the DLR cross-flow 'Prinzipexperiment' (see Bippes 1999, and also Bonfigli & Kloker 2007) and is a model flow for the boundary layer developing on the upper side of a swept-back airplane wing within the region of accelerated flow.

This paper is organized as follows: § 2 presents specific points of the numerical method, § 3 covers the employed base flow and its primary and secondary instability characteristics, and § 4 shows results of various localized-suction scenarios.

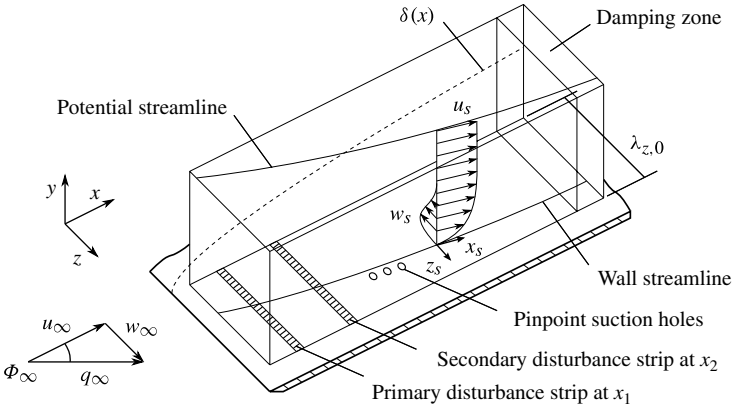

FIGURE 1. Integration domain and coordinate systems.

2. Numerical method

2.1. *Basic set-up*

Our sixth-order accurate finite-difference/Fourier spectral numerical method solves the three-dimensional, unsteady, incompressible Navier–Stokes equations in vorticity–velocity formulation (for details see Wassermann & Kloker 2002) and is proven for weak suction (Messing & Kloker 2010). The reference length $\bar{L} = 0.1$ m and the chordwise reference velocity $\bar{U}_\infty = 14.0$ m s^{-1} ($\bar{Q}_\infty = 19.0$ m s^{-1}) are used for normalization, if not otherwise stated; the overbar denotes dimensional values. Here $\bar{L}$ corresponds to 20 % of the plate's chord length in the 'Prinzipexperiment'. A swept flat plate was used, with a displacement body above inducing a nearly constant favourable chordwise pressure gradient. The global Reynolds number is $Re = \bar{U}_\infty \bar{L}/\bar{\nu} = 92\,000$. The rectangular integration domain consists of Cartesian grid cells. We use x, y and z to denote the chordwise, wall-normal and spanwise directions on the flat plate, as shown in figure 1. The corresponding velocity and vorticity vectors are $\boldsymbol{u} = \{u, v, w\}^{\mathrm{T}}$ and $\boldsymbol{\omega} = \{\omega_x, \omega_y, \omega_z\}^{\mathrm{T}}$. All flow quantities are split into a steady base flow and a disturbance flow $q = q_B + q'$, which are computed successively. This procedure allows adapted boundary conditions to be set in each case. Note that the time mean $\langle q' \rangle$ is non-zero for large q', of course.

In spanwise direction, a Fourier ansatz is used employing K Fourier modes, with the wavenumbers $k\gamma_0$, $k = 0, \ldots, K$ and $\gamma_0 = 2\pi/\lambda_{z,0} = 52.4$; the value $\lambda_{z,0} = 0.12$ is the spanwise extension of the integration domain, corresponding to the wavelength of a strongly amplified CFV mode.

For postprocessing we define a streamline-oriented coordinate system (x_s, y, z_s), where x_s points in the potential-flow direction (ϕ_e) at the upper edge of the integration domain. The respective velocities and vorticities are normalized by the local base-flow edge velocity in the x_s-direction and marked by a tilde, e.g. $\tilde{u}'_s = u'_s/u_{B,s,e}$. Furthermore, an arbitrarily rotated coordinate system (x_r, y, z_r) is defined according to $x_r = (x - x_0)\cos\Phi_r + (z - z_0)\sin\Phi_r$ and $z_r = -(x - x_0)\sin\Phi_r + (z - z_0)\cos\Phi_r$.

For disturbance strips and suction holes at the wall, the wall-normal velocity component can be arbitrarily prescribed. Typically, the disturbance strips are used to excite low-amplitude steady and unsteady disturbances with wavenumbers $k\gamma_0$, frequencies $h\omega_0$, amplitudes $A_{(h,k)}$ and phases $\Theta_{(h,k)}$, where γ_0 and ω_0 are the

fundamental spanwise and timewise wavenumber, respectively:

$$v'(x, y, z, t) = f_v(x) \left(\sum_{k=1}^{K} 2A_{(0,k)} \cos(k\gamma_0 z + \Theta_{(0,k)}) + \sum_{h=1}^{H} \sum_{k=-K}^{K} 2A_{(h,k)} \cos(k\gamma_0 z - h\omega_0 t + \Theta_{(h,k)}) \right). \tag{2.1}$$

Here $f_v(x)$ is a piecewise-defined symmetric fourth-order parabola with zero values, zero first and second x-derivatives at the ends of the respective strip and a maximum value of 1; see Wassermann & Kloker (2002).

For the modelled suction holes, a velocity distribution is prescribed according to

$$v'(x, 0, z) = -v_{max} \cos^3 \left(\frac{\pi r}{d_{mod}} \right), \tag{2.2}$$

where v_{max} is the maximum suction velocity in the hole centre, and r and d_{mod} are the radius and diameter of the modelled hole, with $r = \{(x - x_H)^2 + (z - z_H)^2\}^{1/2}$ and $(x_H, 0, z_H)$ being the hole centre coordinates. For more details of the modelled suction holes, see Messing & Kloker (2010).

Note that a modelled suction-hole velocity distribution needs three parameters to be defined: the maximum suction velocity v_{max}, the hole diameter d_{mod} and the distribution $v(r)$. For the chosen $v(r)$, see (2.2), we need a diameter d_{mod} larger than the d of an assumed Hagen–Poiseuille suction-channel profile, $d_{mod}/d = 1.51$, to yield identical mass flow at the same maximum suction velocity. (Of course, with suction channel included, the velocity distribution will differ from a Hagen–Poiseuille profile locally, however insignificantly with respect to the effect of suction on the flow, see Friederich & Kloker (2011).)

Two-dimensional suction slits with no spanwise variation are prescribed using

$$v'(x, 0, z) = -v_{max} \cos^3 \left(\frac{\pi(x - x_S)}{l_{mod}} \right), \tag{2.3}$$

where x_S defines the slit centre position and l_{mod} the chordwise extension of the slit. Similar to the holes, here a plane Poiseuille flow profile is assumed and hence $l_{mod}/l = 1.57$ to obtain identical mass flow at equal maximum suction velocity, where $l_{mod} = d_{mod}$ has been chosen.

Careful grid studies have shown that for wall suction with, say, $\bar{v}_{max}/\bar{U}_\infty \geqslant 15\,\%$, the resulting gradients of the vorticity components require an extremely fine wall-normal grid at the wall. For suction rates of $\bar{v}_{max}/\bar{U}_\infty = 0.5$, a converged solution is achieved only with Δy_{wall} being three orders of magnitude smaller than $\delta_{1,s}$. Then, simulations with the standard explicit four-step fourth-order Runge–Kutta time integrator are no longer feasible due to the resulting extreme numerical time-step limit dominated by the viscous terms in the wall-normal direction ($\Delta t_{max} \sim \Delta y_{wall}^2$). Therefore, we use a semi-implicit time integration as summarized below.

2.2. *Semi-implicit time integration*

The momentum equations of the Navier–Stokes equations in vorticity–velocity formulation using disturbance values can be written as

$$\frac{\partial \boldsymbol{\omega}}{\partial t} = -\boldsymbol{N} + \frac{1}{Re} \Delta \boldsymbol{\omega} = -\boldsymbol{N} + \boldsymbol{V}, \tag{2.4}$$

where $\boldsymbol{N}$ and $\boldsymbol{V}$ combine the nonlinear and viscous terms, respectively; Δ is the Laplace operator.

In our case the time-step limit is dominated by the term $\boldsymbol{V}_{yy}$ comprising the second wall-normal derivatives of each vorticity component. We implement an implicit time-integration scheme for this term according to the trapezoidal rule. Since this yields $O(2)$ accuracy, a modified Heun method being second-order accurate as well is used for the remaining explicit time integration for full consistency. A second corrector step is added to secure A-stability. The scheme reads

$$\boldsymbol{\omega}^{(l+1)^*} = \boldsymbol{\omega}^{(l)} + \Delta t \left\{ \boldsymbol{R}^{(l)} + \frac{1}{2}\boldsymbol{V}_{yy}^{(l)} + \frac{1}{2}\boldsymbol{V}_{yy}^{(l+1)^*} \right\}, \tag{2.5a}$$

$$\boldsymbol{\omega}^{(l+1)^{**}} = \boldsymbol{\omega}^{(l)} + \frac{\Delta t}{2} \left\{ \boldsymbol{R}^{(l)} + \boldsymbol{R}^{(l+1)^*} + \boldsymbol{V}_{yy}^{(l)} + \boldsymbol{V}_{yy}^{(l+1)^{**}} \right\}, \tag{2.5b}$$

$$\boldsymbol{\omega}^{(l+1)} = \boldsymbol{\omega}^{(l)} + \frac{\Delta t}{2} \left\{ \boldsymbol{R}^{(l)} + \boldsymbol{R}^{(l+1)^{**}} + \boldsymbol{V}_{yy}^{(l)} + \boldsymbol{V}_{yy}^{(l+1)} \right\}, \tag{2.5c}$$

where (l) is the current time level and $\boldsymbol{R}$ substitutes the right-hand side of (2.4) without $\boldsymbol{V}_{yy}$. Each of these equations has the form

$$\left(1 - \frac{\Delta t}{2Re}\frac{\partial^2}{\partial y^2}\right)\boldsymbol{\omega}^{(l+1)} = \tilde{\boldsymbol{R}}, \tag{2.6}$$

where $\tilde{\boldsymbol{R}}$ includes all remaining explicit parts of the right-hand sides of (2.5).

At the wall ($y = 0$), the usual formulations for the wall vorticity are used (see Wassermann & Kloker 2002). They depend on the v-velocity component of the flow field at the new time level, which in turn depends on the new vorticity values here. Thus, an iteration procedure has to be carried out for each substep (2.5*a–c*), monitoring wall vorticity and starting with the wall-vorticity values of the old time level:

$$\left(1 - \frac{\Delta t}{2Re}\frac{\partial^2}{\partial y^2}\right)\boldsymbol{\omega}^{(l+1)^{(i+1)}} = \tilde{\boldsymbol{R}}, \tag{2.7}$$

with (i) being the iteration level. For (2.5*a*), for example, within each iteration step the vorticity components for $y > 0$ are computed, then the v-Poisson equation and finally the wall-vorticity equations are solved. The updated wall values serve as new boundary condition for the next iteration step. Note that the right-hand side $\tilde{\boldsymbol{R}}$ remains constant during the iteration. Five, four and three iteration cycles are used for (2.5*a–c*), respectively.

The convective terms in the y-direction still impose a small time step, translating into an insufficient damping of high-wavenumber modes devised by the alternating forward/backward-biased differencing of the convective terms in the x-direction. Therefore, a compact spatial filter is activated in the x-direction.

2.3. *Verification*

To the best of the authors' knowledge, there are no publications on non-weak, localized suction in three-dimensional boundary layers available. Our numerical method has been well tested and validated for cross-flow transition scenarios as well as for moderate suction in two- and three-dimensional boundary layers (see Messing & Kloker 2010). As verification for strong suction and the modified numerical method, one of the current cases is simulated also with our compressible code that is not based

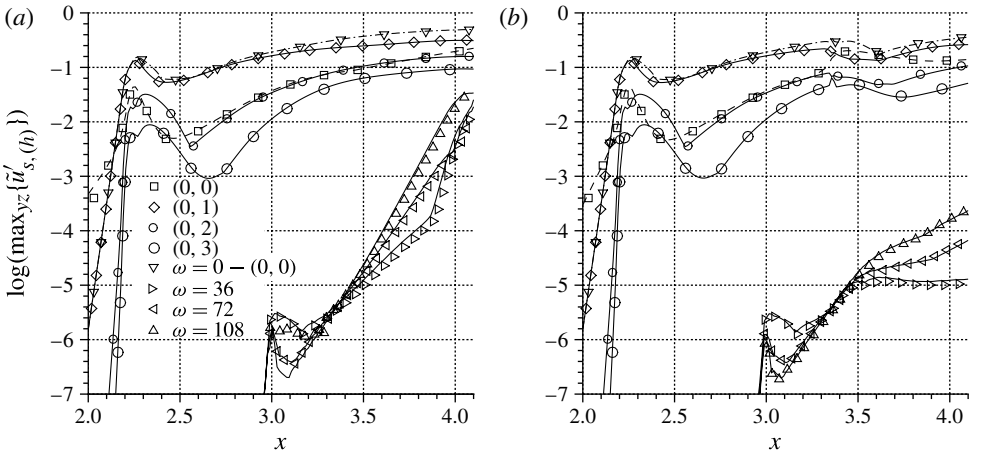

FIGURE 2. Downstream development of selected modal $\tilde{u}'_s$ amplitudes for incompressible code (lines) and compressible code (symbols) for (*a*) a reference case without suction and (*b*) a case with a single suction hole.

Case	N_x	N_y	K	γ_0	$\Delta x \times 10^3$	$\Delta y \times 10^5$	$\Delta z \times 10^3$	$\Delta t \times 10^4$
REF, HOM	3202	209	15	52.4	1.309	7.913/48.238	3.997	1.745
All other	3202	225	15	52.4	1.309	0.659/62.640	3.997	0.655

N_x and N_y represent the number of grid points in x and y direction.
K is the number of the highest Fourier mode in z direction.
Δy is the wall-normal step size at the wall / at $\delta_{s,99}$ ($x = 3.356$).
$\Delta z = 2\pi/(2K\gamma_0)$.
Integration domain: $x \in [1.654, 5.845]$, $y \in [0.000, 0.077]$, $z \in [0.000, 0.1200]$.

TABLE 1. Simulation parameters.

on vorticity. Until now this code has been run with symmetrical two-dimensional base flows and without imposed streamwise pressure gradients. Details of the compressible numerical method, the base-flow calculation and simulation parameters can be found in appendix A.

The wall-normal resolution can be far more coarse for the compressible case: the step size Δy_{wall} is 35 times larger, and only 95 grid points are used compared to 225 for the incompressible case. The wall-normal grid stretching yields $\Delta y_e/\Delta y_{wall} = 12$, versus 120 for the incompressible case. The resolutions in the downstream and spanwise directions ($\Delta x = 1.309 \times 10^{-3}$, $K = 10$) are identical. Still, to obtain a solution at a given physical time after disturbance activation, the incompressible code runs more than 14 times faster when a Mach number of 0.2 is chosen for the compressible case. Note that this does not compare the actual computing time per grid point and time step value.

Figure 2 shows the downstream modal development of the streamline-oriented disturbance velocity component $\tilde{u}'_s = u'_s/u_{B,s,e}$ for a reference case without suction (case REF, see table 1, with $K = 10$) and a case with a single modelled suction hole (case 1-H, $K = 10$; for more details see the next section). In all cases the steady CFV mode with $\gamma = \gamma_0 = 52.4$ has been excited at $x = 2.2$ as primary disturbance and a

packet of controlled unsteady disturbances at $x = 3.0$ has been introduced to check for secondary instability. The match of the results of the two codes proves the correctness of the results at the prescribed boundary conditions and used discretization. Moreover, careful grid studies using higher resolutions, especially $K = 15$ and 21, clearly show that the results in figure 2 are converged.

3. Base flow and its stability properties

The investigated base flow refers to the DLR cross-flow 'Prinzipexperiment' by Bippes and co-workers (see Bippes 1999) and has already been considered and analysed in detail in the DNS work by Bonfigli & Kloker (2007). The nearly constant favourable pressure gradient imposed corresponds to a Falkner–Skan–Cooke flow with a Hartree parameter β_h of approximately 2/3. However, the experimental flow is not truly self-similar and small adaptations are necessary to match the experimental base-flow characteristics, already reported by Bonfigli & Kloker (2007). Boundary-layer parameters are provided in appendix A (figure 16).

The flow is accelerated in the streamwise direction along the whole integration domain, and due to the sweep angle $\Phi_\infty = 42.5°$ the maximum of the cross-flow in the boundary layer increases as well. The shape factor based on the chordwise displacement and momentum-loss thickness is $H_{12} \approx 2.26$ throughout the domain, slightly decreasing.

An investigation using primary linear stability theory (not shown) yields the expected strong instability of the base flow with respect to cross-flow vortex modes. The highest amplification rates are found for unsteady modes ($\omega \neq 0$). Typically, in low-turbulence environments, steady cross-flow vortices are observed due to the higher initial amplitudes of the respective vortex mode and are therefore investigated here. Strong amplification is found for the steady cross-flow vortex mode $\gamma = 52.4 = \gamma_0$, from now on referred to as mode $(0, 1)$ in double-spectral notation. The fundamental frequency $\omega_0 = 6.0$ is the most amplified as for primary instability.

For the DNS, two successive disturbance strips excite steady and unsteady modes with momentum input but without net mass flow by prescribing the wall-normal velocity component at the wall as introduced in (2.1). At $x = 2.2$ the steady mode $(0, 1)$ is triggered whereas at $x = 3.0$ an unsteady, pulse-like disturbance is generated that includes modes $(h, \pm 1)$, $h = 1$–50. Exciting spanwise modes with $\gamma = \pm\gamma_0$ only does not represent a limitation since, together with the vortex modes $(0, 1)$, $(0, 2)$ etc. of the prevailing CFV, the full disturbance spectrum is generated nonlinearly at once.

The downstream modal development of the streamline-oriented disturbance velocity component $\tilde{u}'_s = u'_s/u_{B,s,e}$ for the reference case REF without suction is shown in figure 3. A high initial amplitude of mode $(0, 1)$ is chosen to skip the linear development of the cross-flow vortex mode. The linear stage is extensively discussed in Bonfigli & Kloker (2007) and left out here to save computational resources. (A comparison of the induced CFV shows no notable differences to cases where the fundamental mode was triggered on a lower amplitude level.) At $x = 3.00$ the steady and purely three-dimensional part of the mean flow $\omega = 0 - (0, 0)$, i.e. the steady part of the flow field without the spanwise mean $(0, 0)$, reaches 19 %. Secondary instability sets in immediately, shown by the growth of high-frequency disturbances, e.g. mode $\omega = 120$ ($h = 20$). Starting at $x = 3.75$ nonlinear growth of the low-frequency modes followed by transition to turbulence can be observed.

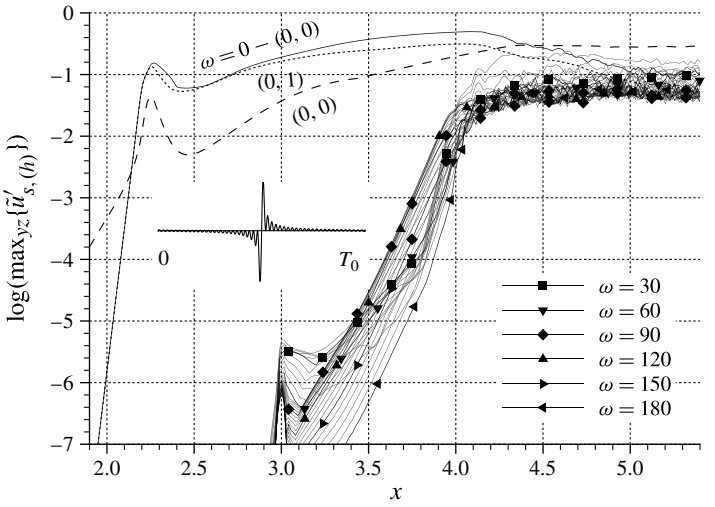

FIGURE 3. Downstream development of modal $\tilde{u}'_{s,(h)}$ amplitudes for case REF from Fourier analysis in time (maximum over y and z, $0 \leqslant \omega \leqslant 180$, $\Delta\omega = 6$). The inset shows the physical time signal of the pulsing.

Note that without unsteady forcing the simulated flow breaks down to turbulence for $x > 5.5$ only. In this case the strong convective secondary instability caused by the large-amplitude CFVs amplifies the small numerical background noise ($O(\tilde{u}'_s) = 10^{-12}$–$10^{-15}$) and it takes until $x = 5.5$ to reach the turbulent state. The forcing of unsteady pulse disturbances has been applied to keep the integration domain short for the various cases considered.

When examining y–z cross-cuts of the $\tilde{u}'_s$ amplitude distribution, we find low-frequency type III modes in the range $6 \leqslant \omega \leqslant 48$, whereas the high-frequency modes ($\omega > 60$) reveal the typical type I or z mode amplitude distributions. (The notation 'y' and 'z' mode follows Malik *et al.* (1999); see also Bonfigli & Kloker (2007).) The high-frequency mode $\omega = 90$ reveals the largest amplitude level at $x = 3.36$. Figure 4 shows its location with respect to the clockwise-turning CFV visualized by $\tilde{u}'_s$ and λ_2 isocontours. The pinpoint-suction set-up is visualized by arrows indicating the prescribed suction velocity at the wall for the later discussed case 1-H with one suction hole.

The suction position shown is (near-)optimal with respect to the attenuation of secondary growth and has been found iteratively. It is not exactly beneath the maximum of the z mode. Note that in a boundary layer with cross-flow the streamline direction varies with the distance from the wall.

4. Influence of pinpoint suction on the flow instability

We consider the following cases within this section: the reference case REF from § 3 is used as the basis for the transition process without suction and for comparison. All remaining cases employ the same disturbance generation but additionally some kind of suction: case HOM shows the effect of homogeneous suction in a chordwise finite area of the integration domain, case 3-S the effect of three successive spanwise suction slits, and cases 1-H, 3-H, 3-H* and 9-H are set up with one, three, or nine successive suction holes at the wall, positioned along the CFV.

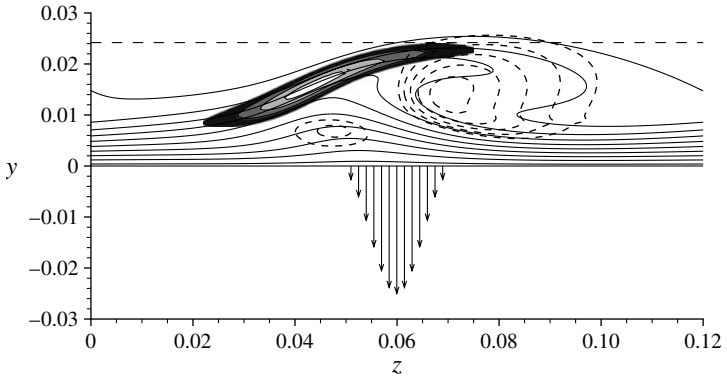

FIGURE 4. Pinpoint suction set-up: cross-cut at $x = 3.356$ for case REF. Solid lines show $\tilde{u}_s$ isocontours (0.05–0.95, with increment 0.1); and dashed lines show λ_2 isocontours (−25 to −5, with increment 5). The modal $\tilde{u}'_s$ amplitude distribution for high-frequency secondary instability mode $\omega = 90$ is visualized by grey scale (0.3–0.9, with increment 0.2). Arrows show the pinpoint-suction distribution at the wall as applied for case 1-H (cross-cut through centre of suction hole). The horizontal dashed line denotes the undisturbed boundary-layer thickness $\delta_{s,99}$.

Case	Suction set-up	v_{max}	v_{avg}	c_q	$d \times 10^2$	Suction centre at x_H
REF	—	—	—	—	—	—
1-H	1 hole	0.5000	0.2500	$c_{q,0}/3$	1.73	3.36
3-H, 3-H*	3 holes	0.5000	0.2500	$c_{q,0}$	1.73	3.36, 3.38, 3.40
9-H	9 holes	0.5000	0.2500	$3c_{q,0}$	1.73	3.36, 3.38, …, 3.52
3-S	3 slits	0.0441	0.0295	$c_{q,0}$	$l = 1.67$	3.36, 3.38, 3.40
HOM	homogeneous	0.0016	0.0016	$c_{q,0}$	—	3.15–4.05

Reference suction coefficient $c_{q,0} = 1.6 \times 10^{-3}$.
$v_{max} = \bar{v}_{max}/\bar{U}_\infty$, $v_{avg} = \bar{v}_{avg}/\bar{U}_\infty$.

TABLE 2. Simulation set-ups. For all simulations, disturbance strips trigger the primary vortex mode $(0, 1)$ with an amplitude of $A = 9.30 \times 10^{-3}$ at $x_1 = 2.20$ and the background pulse including modes $(1, \pm 1)$–$(50, \pm 1)$ with an amplitude of $A = 6.25 \times 10^{-7}$ at $x_2 = 3.00$. The spanwise location of suction-hole centres for cases 1-H, 3-H and 9-H is $z_H = 0.5\lambda_{z,0} = 0.06$.

Table 1 summarizes the numerical parameters for the various cases, and table 2 gives parameters for disturbance and suction generation.

4.1. *Downstream development of disturbances and transition delay*

First, the homogeneous suction case is considered. We define a suction coefficient using the free-stream velocity in chordwise direction by

$$c_q = \frac{\bar{v}_{avg} P}{\bar{U}_\infty}, \tag{4.1}$$

where $\bar{v}_{avg} = (1/A) \int v \, \mathrm{d}A$ (A being the orifice area) is the average suction velocity over the suction orifice and P the porosity of the suction panel. A value

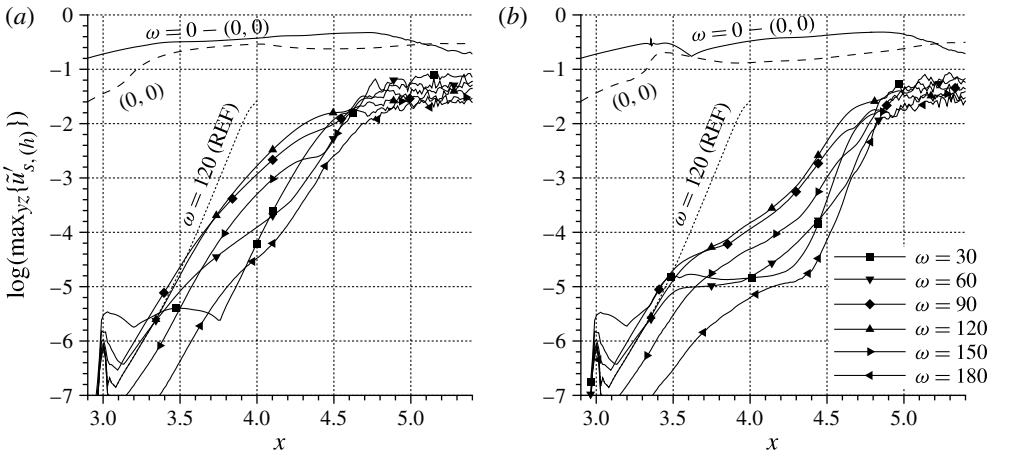

FIGURE 5. Downstream development of modal $\tilde{u}'_{s,(h)}$ amplitudes from Fourier analysis in time (maximum over y and z, $0 \leqslant \omega \leqslant 180$, $\Delta\omega = 30$) for cases (*a*) HOM and (*b*) 1-H. Mode $\omega = 120$ from case REF has been added as reference (dotted line).

of $c_{q,0} = 1.6 \times 10^{-3}$ on a chordwise extension of the suction domain of $l_x = 0.9$ is chosen for case HOM. The homogeneous suction operates at $v = v_{max} = 0.0016$ ($P = 1$) and covers the complete spanwise domain. The increase of the spanwise mean $(0, 0)$ between $3.15 \leqslant x \leqslant 4.05$ in figure 5(*a*) is a consequence of the homogeneous suction. Little influence on the main vortex ($\omega = 0 - (0, 0)$) is observed. A slight reduction of secondary amplification is found for all considered high-frequency modes compared to the selected reference mode $\omega = 120$ from case REF that gained the highest amplification rate. However, transition to turbulence is only marginally delayed.

The first pinpoint-suction case 1-H is set up by selecting the location of the suction-hole centre ($x_H = 3.356$, $z_H = 0.060$) and the hole diameter of $d = 0.0173 = 2.30\delta_{1,s}(x_H)$. The maximum suction velocity is $v_{max} = \bar{v}_{max}/\bar{U}_\infty = 0.5$, corresponding to $v_{max}/u_{B,s,e} = 0.413$. The hole is located according to figure 4 as discussed above. Slight variations of the spanwise location of the hole centre have only a minor influence on the attenuating effect of the suction.

If the reference area from case HOM is considered ($A_{hom} = \lambda_{z,0}\, l_x$), the porosity for case 1-H yields $P = (\pi d^2/4)/A_{hom} = 0.0022$ and the suction coefficient results in $c_q = 5.45 \times 10^{-4}$, which is approximately $c_{q,0}/3$.

The localized suction influences the vortex strength, see figure 5(*b*). The y–z maximum of the steady, three-dimensional $\tilde{u}'_s$ deformation of the flow ($\omega = 0 - (0, 0)$) shows a significant reduction behind the suction hole, its amplitude dropping from 0.30 to 0.17. Secondary growth of all modes is affected immediately and significantly reduced. Only after $x = 4.3$ are the former amplification rates regained due to the regrown CFV.

The influence of the diameter and the mass and momentum input are summarized in appendix B. We find that the mass flux sucked is the most important parameter with respect to attenuation of secondary growth, rather than the maximum suction velocity and thus the wall-normal momentum output.

To increase the sucked mass flow, we add more holes to prevent oversuction caused by one hole with an unduly large suction velocity $\bar{v}_{avg}$. Three successive suction holes,

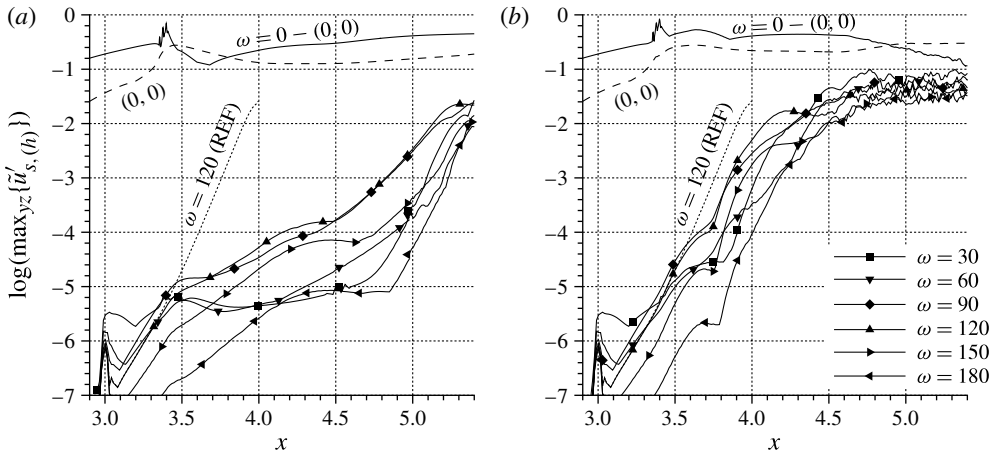

FIGURE 6. Like figure 5 but for cases (*a*) 3-H and (*b*) 3-H*.

each with the same suction parameters as the single hole in case 1-H, are set up, resulting in $c_q = c_{q,0}$. The hole centres are aligned in a straight line, parallel to the vortex-core orientation at $x = 3.36$. Results for the case 3-H are provided in figure 6(*a*). In spite of a local increase, the vortex amplitude level is reduced to 0.12 at $x = 3.7$, and stronger attenuation of secondary growth can be observed for all unsteady modes. Transition is shifted to the end of the considered domain. Note that one length unit ($\bar{L} = 0.1$ m) corresponds to $133\delta_{1,s}$ at $x = 3.36$.

In order to check the influence of the spanwise suction-hole position, case 3-H* is set up with all suction holes shifted by $\lambda_{z,0}/2$. This is pessimal considering the spanwise spacing and sense of rotation of the CFVs. Figure 6(*b*) shows indeed an enhancement of the CFV strength to a maximum value of more than 53 % at $x = 3.65$. However, the overall effect of the suction seems to overcome the misalignment drawback, and transition is at least not enhanced. Therefore we conclude that a varying spanwise location of the suction holes can either enhance or weaken the CFV amplitude, but secondary instability is always weakened due to deformation of the CFV and the mean suction effect, pulling the flow to the wall.

To further investigate the role of the spanwise position of suction, case 3-S with three consecutive spanwise slits is set up at the same chordwise locations as for case 3-H. No spanwise variation of suction is present, but in contrast to case HOM it is localized in the chordwise direction. With our spectral code this is simply achieved by neglecting $v'_k(y = 0)$ for $k > 0$, since the spanwise slit represents the spanwise mean component $v'_{k=0}(y = 0)$ of a case with suction holes; $c_q = c_{q,0}$ like for the cases HOM and 3-H. Figure 7(*a*) shows that the resulting transition delay lies in between cases 1-H and 3-H. The chordwise concentration of suction improves transition delay compared to homogeneous suction; however, the slit suction does not perform as well as case 3-H at identical c_q values.

Finally, nine consecutive holes are arranged in a straight line parallel to the vortex-core orientation at $x = 3.36$, employing $c_q = 3c_{q,0}$. Secondary growth and thus transition to turbulence is eliminated completely; see figure 7(*b*). The downstream regrowth of the CFV pulled to the wall is apparently too small to provoke secondary instability inside the considered domain. In order to enable the formation of possibly new instability modes, the disturbance pulse from $x = 3.0$ is repeated at $x = 4.0$ and $x = 4.5$. No secondary growth is observed.

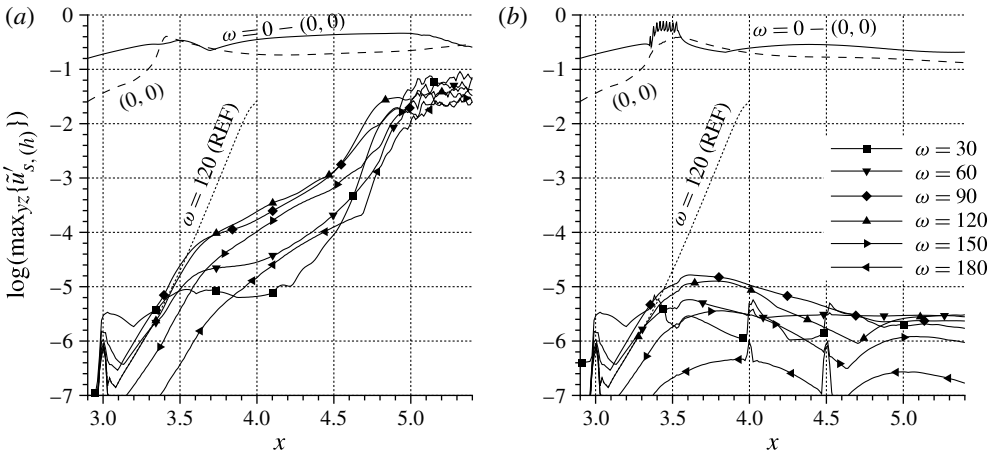

FIGURE 7. Like figure 5 but for cases (*a*) 3-S and (*b*) 9-H.

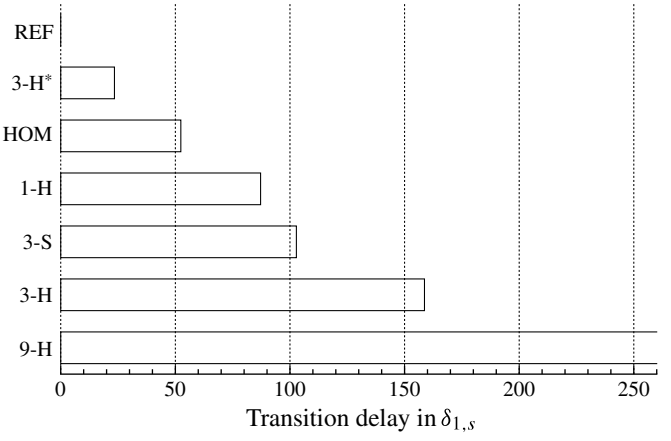

FIGURE 8. Transition delay of all cases. Downstream locations are taken where the largest unsteady mode reaches a $\tilde{u}_s$ amplitude of 10^{-2}. Reference displacement thickness of the undisturbed base flow: $\delta_{1,s}(x = 4.00) = 7.73 \times 10^{-3}$.

Figure 8 provides a comparison of the transition delay for all cases. The amplitude level of $\tilde{u}'_s = 10^{-2}$ of the largest unsteady mode is used to measure the (relative) transition shift. Case 1-H is almost as efficient as case 3-S although c_q is three times smaller. Case 3-H shows a 50 % larger transition delay compared to case 3-S at identical suction rates. For case 9-H onset of transition cannot be detected in the considered domain.

4.2. *Skin friction development*

Figure 9 shows the parameter $C(x) = \int \max_t\{\partial u_{42.5°}/\partial y|_{y=0}\}\,\mathrm{d}x$. The gradient of the spanwise mean flow in flight direction $\partial u_{42.5°}/\partial y|_{y=0}$ is proportional to the skin friction coefficient. In order to account for fully turbulent flow, we take the maximum value within one fundamental period of time in our simulation with pulsed disturbances.

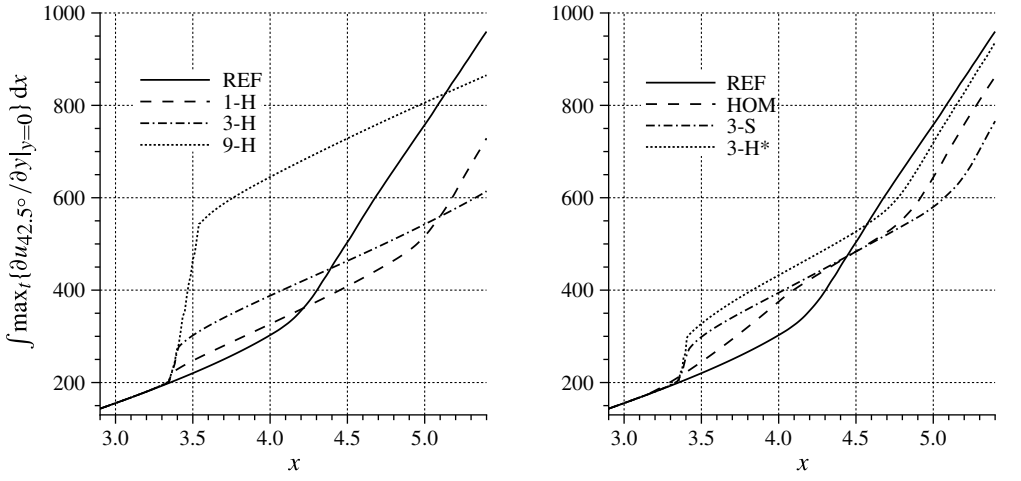

FIGURE 9. Downstream development of the (in streamwise direction) integrated wall-normal velocity gradient of the spanwise mean velocity component in the direction of the oncoming flow ($\Phi_\infty = 42.5°$) at the wall, serving as a measure of the skin friction coefficient c_f. For the integration, the maximum over one fundamental period in time has been used in order to account for a fully turbulent flow (and not pulsed transition).

Parameter $C(x)$ allows for direct comparison of the curves at chordwise locations. The reference case reveals laminar flow up to $x = 4.0$. The change in slope indicates transition to turbulent flow. Case 1-H shows the skin friction increase caused by suction, pulling high-momentum fluid to the wall, at $x = 3.36$. However, at $x = 4.2$ the increase is compensated by sustaining laminar flow and less skin friction can be found throughout the integration domain in spite of turbulent flow starting at $x = 5.0$.

For case 3-H the approximately three times higher increase occurring at $x = 3.5$ arises from the three consecutive holes and thus three times larger mass flow sucked. However, for $x > 5.1$ this case causes less friction drag than case 1-H. Case 9-H shows an enormous increase around $x = 3.5$ but the flow stays laminar for so long that it will eventually outperform all other cases. Cases HOM, 3-S and 3-H* provide similar results as case 1-H with different locations of transition to turbulence. Note that further effects like the influence of the suction on the pressure distribution (sink effect) or the power required for the suction system have not been taken into account in this evaluation. (We note that suction without additional pumps is currently investigated in practice. In this case the suction areas are connected to regions of low pressure on an aircraft.)

4.3. *Vortical structures*

Figure 10 shows visualizations of vortical structures for five selected cases in a rotated reference system. The angle $\Phi_r = 45.0°$ has been chosen to approximately straighten the CFVs in the visualization. The snapshot for case REF shows nearly undisturbed flow up to $x_r = 1.3$. The small structures at $x_r = 0.8$, $z_r = 0.08$ show the disturbance pulse in an early stage. The turbulent region between $x_r = 1.5$ and $x_r = 2.0$ is caused by the previous pulse.

For case 3-H the suction holes are marked by black circles. We expect a counter-rotating vortex pair developing behind the suction orifices such that each vortex 'transports' fluid into the hole. In a top view, the vortex emerging to the right turns

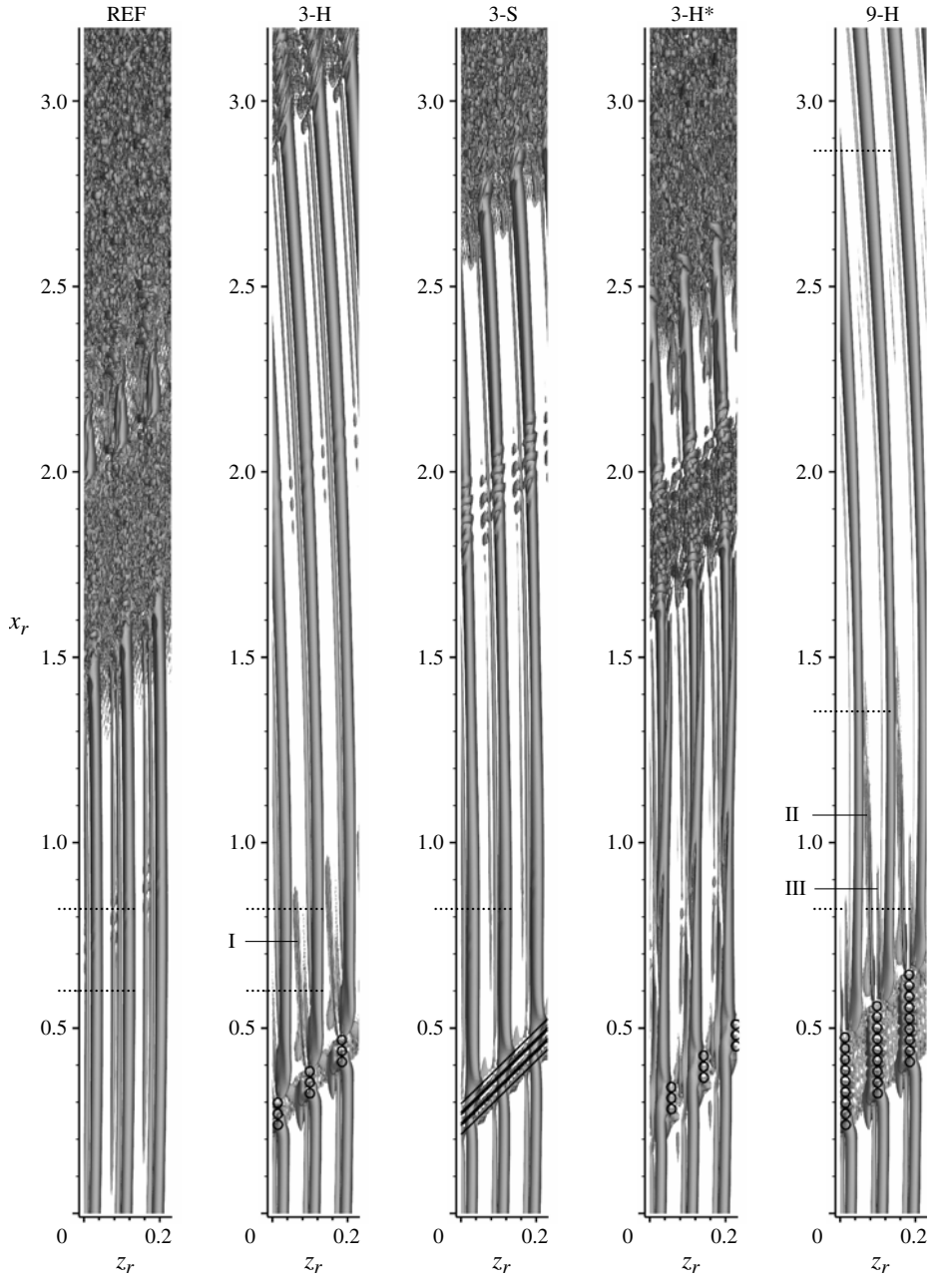

FIGURE 10. Vortex visualization ($\lambda_2 = -1$), top view, snapshot in time, to scale. A rotated reference system is used with $x_0 = 3.2$, $z_0 = 0$ and $\Phi_r = 45.0°$. Dotted lines refer to cross-cuts of figures 11–14. Approximately three fundamental spanwise wavelengths are shown.

anticlockwise, i.e. close to the wall against the cross-flow direction, and thus dies out soon in this case and cannot be discerned (cf. Messing & Kloker 2010). The one emerging to the left (structure I) turns in clockwise direction like the oncoming CFV, is shifted to the left and suppressed by the CFV shortly before merging with it. The

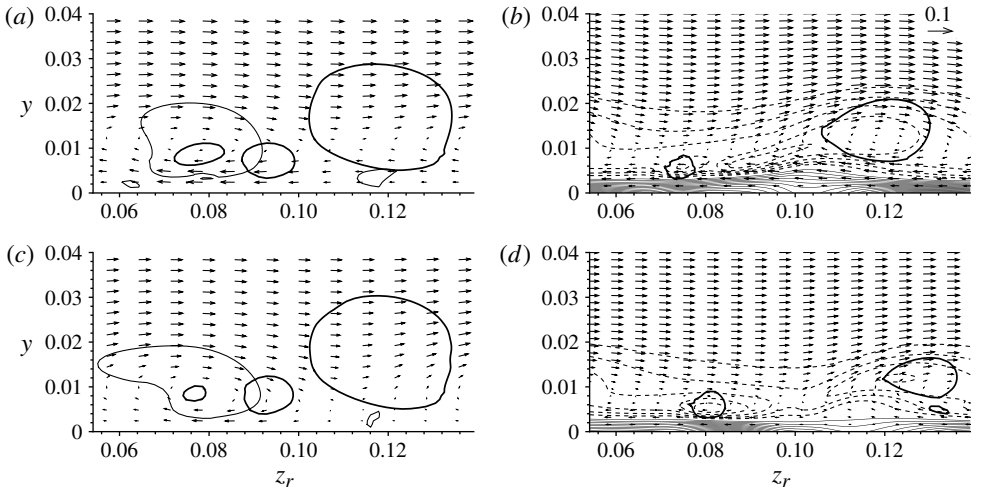

FIGURE 11. Cross-cuts: (*a*) 3-H-noCFV, $x_r = 0.60$ ($x \approx 3.62$); (*b*) 3-H, $x_r = 0.60$ ($x \approx 3.62$); (*c*) 9-H-noCFV, $x_r = 0.82$ ($x \approx 3.78$); and (*d*) 9-H, $x_r = 0.82$ ($x \approx 3.78$). Panels (*a*) and (*c*) show isocontours with $\lambda_2 = -2$ (thin lines; case REF added with thick lines) and $[\tilde{w}_r, \tilde{v}]$ vectors; panels (*b*) and (*d*) show $\tilde{\omega}_{x,r}$ isocontours (lines, with increment 2, dashed negative values, zero level not shown). The rotated reference system from figure 10 is used.

oncoming CFV persists and is marginally shifted in positive spanwise direction. The secondary structures from the pulsing are on much lower amplitude levels compared to case REF.

Case 3-S shows local dislocation to the left and deformation of the oncoming CFV above the suction slits but the spanwise location downstream is not altered at all. (The local, opposite dislocation at the beginning and end of suction might be caused by the oblique slit orientation with respect to the CFV axis.) Secondary structures are more pronounced than in case 3-H.

Case 3-H* with pessimal suction-hole locations shows strong deformation of the primary vortices and only marginal transition delay.

Case 9-H shows strong downstream effects of the nine consecutive suction holes and a strong positive spanwise shift of the oncoming CFVs. Similar to case 3-H the left co-rotating vortex emerging from the suction holes can be clearly seen (structure II), this time almost merging with the CFV. The counter-rotating, right suction vortex, structure III, does not die out soon but is strong enough to push the oncoming CFV to the right before it is swallowed by the cross-flow. No structures from the pulse are visible in the considered domain. For the full dynamics of the flow structures for cases 3-H, 3-H* and 9-H, see the supplementary movies with the online version of the paper available at http://dx.doi.org/10.1017/jfm.2012.269.

We note that in case 9-H turbulence does not occur near $x \approx 5.5$ ($x_r \approx 3.3$) as discussed for case REF, in the latter caused by amplification of numerical background noise. In case 9-H secondary instability is absent, and unsteady disturbances do not grow, or only grow very weakly.

4.4. *Cross-cuts: vortices*

To clarify the mechanisms occurring downstream of the suction holes, cross-cuts are considered in figure 11. A case like case 3-H but without oncoming CFV and without

pulse is considered (case 3-H-noCFV) to identify the flow field induced by suction in the undisturbed base flow. Figure 11(*a*) shows λ_2 isocontours in the plane $x_r = 0.600$ from figure 10 for case REF (thick lines) and case 3-H-noCFV (thin lines). The CFV centre can be found at $z_r = 0.117$, the centre of the co-rotating left suction-induced vortex at $z_r = 0.078$. Figure 11(*b*) shows the same cross-cut for case 3-H to clarify the 'nonlinear superposition'. The persisting main vortex sits at $z_r = 0.120$, is much weaker, and the co-rotating suction-hole induced structure can be found at $z_r = 0.074$. Note the negative values of $\tilde{\omega}_{x,r}$, confirming the sense of rotation.

The same procedure is carried out for case 9-H with cross-cuts at $x_r = 0.824$. Figure 11(*c*) provides results for case REF and case 9-H-noCFV showing the respective spanwise vortex locations. Figure 11(*d*) clearly reveals the positive spanwise shift of the CFV. The nine consecutive holes induce a stronger vortex pair where: (i) the persisting left one suppresses the oncoming CFV sufficiently enough to cancel secondary instability; and (ii) the right one pushes the CFV to the right where the CFV is at the same time closer to the wall due to the stronger suction. The specific action of three-dimensional pinpoint suction on the flow is the generation of a vortex co-rotating with and situated in between the oncoming CFVs, thus weakening them (cf. the UFD effect described by Wassermann & Kloker (2002)). Of course, the two-dimensional suction effect is the basis for this. It pulls the flow to the wall, thereby weakening spanwise gradients as discussed below.

4.5. *Cross-cuts: eigenfunctions*

The influence of suction on the u_r amplitude distribution of secondarily unstable eigenmodes becomes evident in figure 12. For case REF the low-frequency mode $\omega = 30$ of type III can be found below the main vortex connected to the local maximum spanwise gradient, whereas the high-frequency mode $\omega = 120$ is connected to the local minimum and hence a type I or z mode. We focus on the z mode since it has the largest amplification rates. Usually, its maximum is also connected to the maximum wall-normal gradient. Figure 12(*b*) displays distributions of the spanwise and wall-normal gradients of the downstream velocity component $\tilde{u}_r$ multiplied by the wall-normal coordinate y to downgrade near-wall maxima that are not relevant. At the maximum of the eigenfunction we find $u_{z,max} = y(\partial u_r/\partial z_r)/u_{B,s,e} = |-1.21|$ and $u_{y,max} = y(\partial \tilde{u}_r/\partial y) = 1.00$. Case 3-S reveals a changeover to a y mode, with $u_{z,max} = |-0.38|$ and $u_{y,max} = 1.12$. The spanwise mean suction reduces the overall spanwise shear by pulling the vortex towards the wall. For case 3-H we find $u_{z,max} = |-0.16|$ and $u_{y,max} = 0.77$. The hole suction deforms the vortex such that the flow gradients are additionally reduced. The impact on the main vortex can be found when comparing the three λ_2 distributions where case 3-H shows the weakest main vortex. If we compare the value $\sqrt{u_z^2 + u_y^2}|_{max}$ for cases REF, 3-S and 3-H, we find 1.57, 1.18 and 0.79, respectively, indicating an overall shear reduction, suggesting a direct measure for attenuation of secondary growth. When comparing the amplification rates of mode $\omega = 120$ at $x = 3.78$ from figures 6(*a*) and 7(*a*), it turns out that the growth rates for cases 3-S and 3-H are almost identical, with the amplitudes lower for case 3-H. In other similar cases not shown, also the secondary growth rates decrease with decreasing gradient.

An evaluation of case 9-H (figure 13) shows a similar trend. The frequency $\omega = 90$ is chosen instead of $\omega = 120$ as for figure 12 since it has the highest amplitude level. Now $\sqrt{u_z^2 + u_y^2}|_{max}$ yields the values 0.41, 0.82 and 0.71 at the three downstream positions shown. Using nine holes consequently further reduces the main

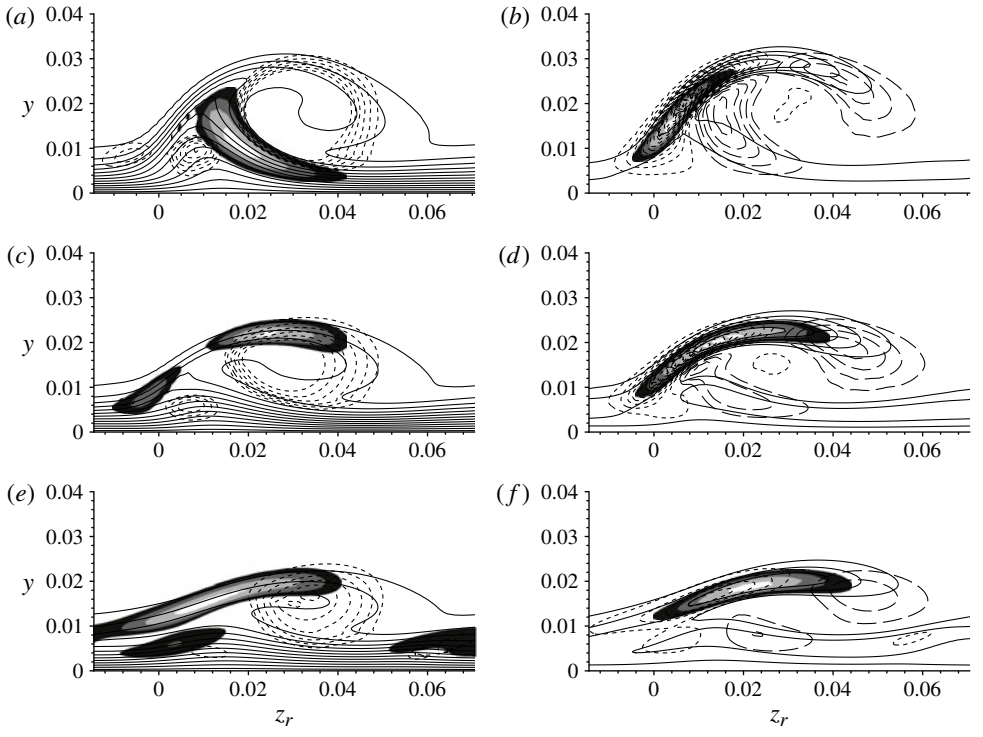

FIGURE 12. Cross-cuts at $x_r = 0.82$ ($x \approx 3.78$): (*a*,*b*) REF; (*c*,*d*) 3-S; (*e*,*f*) 3-H. Panels (*a*,*c*,*e*) show $\tilde{u}_r$ isocontours (lines, 0.05 to 0.95, with increment 0.075), λ_2 isocontours (dashed lines, -2 to -12, with increment 2) and the normalized u_r amplitude distribution for mode $\omega = 30$ (shaded, levels 0.3 to 0.9, with increment 0.2). Panels (*b*,*d*,*f*) show $y(\partial u_r/\partial z_r)/u_{B,s,e}$ isocontours (solid lines, increment 0.2, increment 0.4 for case REF) and $y(\partial \tilde{u}_r/\partial y)$ isocontours (short-dashed, positive; long-dashed, negative values; zero level not shown, increment 0.05, increment 0.10 for case REF) and normalized u_r amplitudes for mode $\omega = 120$. The rotated reference system from figure 10 is used.

flow gradients, but predicting secondary stability is difficult employing this criterion. The development of the low-frequency mode shows a non-amplified TS-like amplitude distribution since no distinguished spanwise gradients exist. The development of mode $\omega = 90$ tends to switch from a z mode to a y mode. All modes shown are damped or neutral.

4.6. *Cross-cuts: Kelvin–Helmholtz shear*

To find a measure for secondary amplification, we follow a procedure described by Bonfigli & Kloker (2007). A shear-layer plane, oriented perpendicular to the axes of the secondary vortex structures – direction t – is obtained by artificial amplification of the respective u, v and w eigenmodes and visual inspection of the corresponding secondary λ_2 structures. Here t is roughly, but essentially not exactly, the direction of the CFV axis. Figure 14 shows the vorticity component $\omega_{x,t}$ perpendicular to the Kelvin–Helmholtz (KH) shear-layer plane for four cases. (We note that there is a labelling error for ϕ_t in figure 33 of Bonfigli & Kloker (2007). The correct sketch is shown as the inset in figure 14*d* of the current paper.) The values found here provide the expected information. Evaluating $w_{x,t}$ at the respective eigenfunction maximum

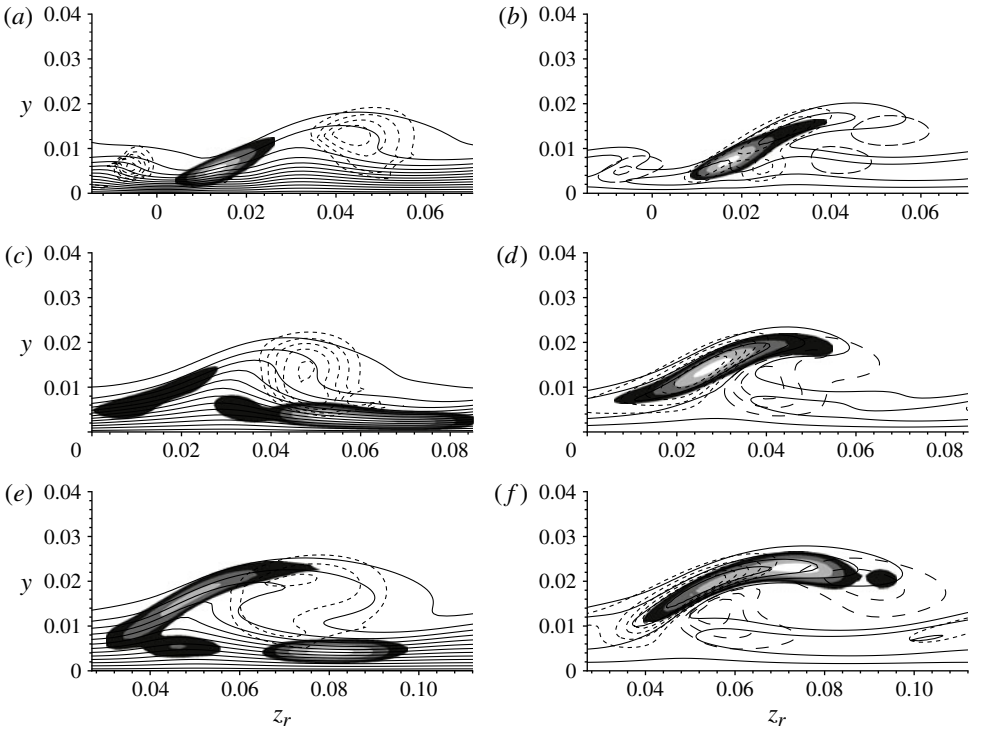

FIGURE 13. Cross-cuts for case 9-H: (*a*,*b*) $x_r = 0.82$ ($x \approx 3.78$); (*c*,*d*) $x_r = 1.36$ ($x \approx 4.19$); and (*e*,*f*) $x_r = 2.87$ ($x \approx 5.23$). Panels (*a*,*c*,*e*) show mode $\omega = 30$; panels (*b*,*d*,*f*) show mode $\omega = 90$. See figure 12 for details.

delivers the following values for cases REF, 3-S, 3-H and 9-H: 61.5, 40.0, 37.5 and 7.6. Evidently, lower KH shear-layer strength yields smaller secondary amplification. For all cases, $\omega_{x,t}$ at the respective eigenfunction maximum is composed primarily of a combination of ω_y and $\omega_{z,r}$. For cases 3-S and 3-H, ω_y basically determined by $\partial u_r/\partial z_r$ is significantly reduced. Additionally, for case 3-H, the KH plane is tilted more relative to the plane perpendicular to the CFV axis ($\psi_t = 10°$), and thus the contribution of ω_y is additionally decreased. Although the contribution of $\omega_{z,r}$ and thus $\partial u_r/\partial y$ to the $\omega_{x,t}$ value is enhanced with increasing angle ϕ_t for cases 3-S and 3-H, this effect is overcompensated by the decreased wall-normal vorticity component. This causes a changeover from a z mode (figure 14*a*) to a y mode (figure 14*c*) comparing the respective location of the eigenfunction maximum in figure 14. The evaluation for case 9-H is added to show the virtually vanishing $\omega_{x,t}$ component. The strongly altered orientation of the t plane of a damped mode is of minor relevance. Also, a velocity component normal to the shear layer in its plane further reduces the instability; see Bonfigli & Kloker (2007). However, to gain reliable *a priori* information on secondary instability properties, a two-dimensional eigenfunction solver, a comprehensive method using the parabolized stability equations (PSE), or DNS is required.

5. Conclusions

The effects of localized, concentrated suction at the wall on the secondary instability of a laminar, cross-flow-dominated boundary-layer flow deformed by grown cross-

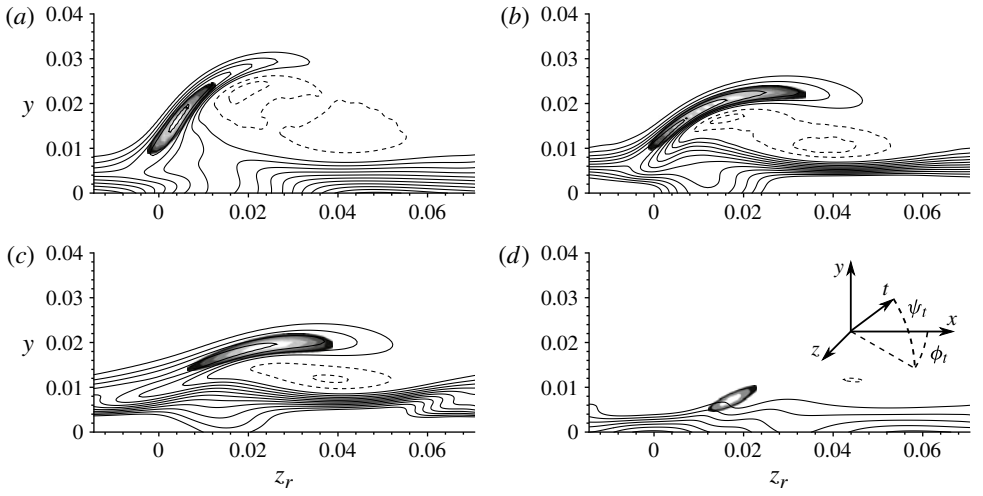

FIGURE 14. Cross-cuts at $x_r = 0.82$ ($x \approx 3.78$): (*a*) REF, $\phi_t = 66°$, $\psi_t = 15°$, (*b*) 3-S, $\phi_t = 91°$, $\psi_t = 16°$, (*c*) 3-H, $\phi_t = 105°$, $\psi_t = 10°$, and (*d*) 9-H, $\phi_t = 54°$, $\psi_t = 7°$. Vorticity component $\omega_{x,t}$ (lines, increment 10, dashed negative values, zero level not shown) and normalized u_r amplitude distribution (shaded, levels 0.5–0.9 with increment 0.1) for mode $\omega = 120$ ($\omega = 90$ for case 9-H). See the inset in (*d*) for the definition of the direction t. Note that ϕ_t is measured in the chordwise system and $\Phi_r \approx 45.0°$ has to be subtracted in order to get the relative angle to the CFV axis direction. The rotated reference system from figure 10 is used.

flow vortices (CFVs) have been investigated by DNS. The main findings can be summarized as follows.

(i) Suction can successfully stabilize not only quasi-two-dimensional base flows with respect to primary instability, which is the classical application of suction in laminar flow control, but also fully three-dimensional boundary layers with large-amplitude CFVs, arising from primary cross-flow instability. Then secondary instability is controlled.

(ii) The first, two-dimensional effect is pulling the CFVs to the wall, thereby flattening them and reducing spanwise shear. Simultaneously, the effect of local extrema of wall-normal shear is reduced because their distance to the wall is diminished. Thus secondary instability is weakened.

(iii) The second effect appears if suction is concentrated not only in chordwise but also in spanwise direction, namely if it is positioned near the updraft side of each CFV where the maximum amplitude of the secondary disturbances is situated. At first it may be thought that suction then directly weakens the rotational fluid motion caused by the CFV, but it turns out that suction induces a pair of counter-rotating vortices. If looking downstream and with a basic cross-flow to the left, the right suction vortex has a rotation opposite to the CFV, and is suppressed shortly downstream by the basic cross-flow – not depending much on the existence of the CFV. It can, however, push the CFV away from the suction hole to the right. The left suction vortex rotates like the CFV, hampering it due to its closeness, before it is eventually suppressed by it. Hence the effect on the flow is different from two-dimensional, symmetrical base flows where the (partial) cancellation of an oncoming vortex is caused by an antiphase/counter-rotating vortex.

(iv) The consequence of the flow alterations is a significant change of the secondary stability properties. The travelling secondary vortices are oriented more parallel to the cross-flow direction, i.e. a changeover from type I (z) modes to type II (y) modes is forced, and the vertical angle between their axis and the axes of the CFVs is reduced. Since the shear in the respective (KH) plane perpendicular to their axes is significantly reduced, their amplification is substantially attenuated, or even halted.

(v) With nine successive holes along the CFV, each having a diameter of about twice the displacement thickness, and a suction velocity of $\sim$20 % of the external velocity, averaged over the hole, complete suppression of secondary instability is achieved in an example. This corresponds to 36 conventional suction holes (with a diameter d of one displacement thickness) and a 2–3 times higher than usual suction velocity averaged over one hole. Thus, the suction rates applied for 'pinpoint' suction are distinctly below the values that might cause local flow tripping. (Our own tentative DNS investigations on so-called oversuction caused by single holes indicate that, for the parameters $Re_{\delta_{1,s}}$ and $d/\delta_{1,s}$ used, the critical suction velocity $\bar{v}_{avg}/\bar{u}_{b,s,e}$ lies beyond 45 %.)

(vi) The increase of the wall shear by the concentrated suction is non-negligible but is far outweighed by the substantial transition delay.

(vii) For practical applications of pinpoint suction, either the position of the CFVs with respect to the suction holes has to be fixed – for example, by using controllable actuators upstream – or the slit version may be applied, but that is less effective. Note that only a few spanwise slits would be necessary.

Acknowledgements

The supercomputing time provided by the Federal High-Performance Computing Center Stuttgart (HLRS) within project LAMTUR is gratefully acknowledged.

Supplementary movies

Supplementary movies are available at http://dx.doi.org/10.1017/jfm.2012.269.

Appendix A. Compressible DNS code and compressible base flow

Our compressible code is used to verify the incompressible results. The numerical method is briefly described in § A.1 and the base-flow computation is summarized in § A.2. Section A.3 gives the numerical parameters of the compressible simulation.

A.1. *Compressible numerical method*

The three-dimensional unsteady compressible Navier–Stokes equations are solved together with the continuity and energy equations in conservative formulation, where $\boldsymbol{Q} = (\rho, \rho u, \rho v, \rho w, E)^{\mathrm{T}}$ represents the solution vector. The coordinate systems are identical to the incompressible ones. The specific heat capacities c_p and c_v as well as the Prandtl number are assumed to be constant, whereas the temperature–viscosity dependence is modelled by Sutherland's law.

The following boundary conditions are employed based on an existing initial flow field that is designated as base flow. At the subsonic inflow, all base-flow variables are prescribed and upstream-travelling acoustic waves are allowed to leave the integration domain. The no-slip isothermal wall with pressure extrapolation for the wall pressure using $\partial p/\partial y|_{wall} = 0$ includes several disturbance strips where the wall-normal mass flux component is prescribed to excite steady and unsteady disturbances, similarly

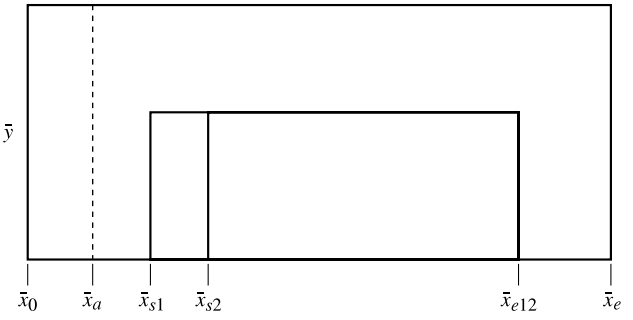

FIGURE 15. Sketch of the integration domain extensions for base-flow computations. Not to scale. PNS domain from $\bar{x}_0$ to $\bar{x}_e$. DNS domains from $\bar{x}_{s1}$, $\bar{x}_{s2}$ to $\bar{x}_{e12}$.

to the incompressible code. At the outflow a buffer domain is employed that ramps all conservative variables to their respective base-flow values. At the free stream the base-flow values are kept for w, T and ρ, suppressing all disturbances. In addition, $\partial u/\partial y|_e = 0$ allows u_e to adequately adapt, and $\partial v/\partial y|_e = -(\partial(\rho_e u_e)/\partial x)/\rho_e$ is exploited to get v_e, assuming $\partial\rho/\partial y|_e = 0$.

Sixth-order compact finite differences on an orthogonal, but stretched, grid are used to discretize the streamwise and wall-normal directions. For the spanwise direction, a Fourier spectral ansatz is implemented to compute the spanwise derivatives. The explicit four-step fourth-order Runge–Kutta scheme serves as time integrator. All equations are solved in total variables. Standard normalization is used with reference length $\bar{L}$, velocity $\bar{U}_\infty$, temperature $\bar{T}_\infty$ and density $\bar{\rho}_\infty$. An extensive description of the numerical method can be found in Babucke *et al.* (2006).

A.2. *Compressible base flow*

For small Mach numbers the viscous part of the numerical time step limit typically is dominating and requires a time step proportional to Ma_∞^2. For the considered case the Mach number of the experiment is $Ma_\infty \approx 0.05$, being computationally too prohibitive. Therefore, $Ma_\infty = 0.21$ has been chosen. To ensure comparable flow regimes, the Re_{δ_1} ranges are matched.

The compressible base flow is obtained in two steps. First, a solution of the three-dimensional compressible parabolized Navier–Stokes (PNS) equations with constant spanwise free-stream velocity and prescribed streamwise pressure gradient is computed using an extension of the PNS code originally developed by Schmidt (see Schmidt & Rist 2011). This PNS solution serves as initial and boundary conditions for the second step, the steady full Navier–Stokes computation, cf. figure 15.

This procedure is necessary for three reasons. Appropriate boundary conditions of the final DNS domain at the inflow and the upper boundary are required, preventing significant streamwise transients in this DNS domain. Also, the integration domain of the (numerically cheap) PNS solution is huge in order to prevent influences of the *ad hoc* chosen inflow boundary onto the final DNS domain. Last, matching the flow to the incompressible case required many iterations, suggesting a fast numerical procedure.

As for the PNS, the dimensionless free-stream velocity distribution $u_e(x)$ is chosen as design variable and matched to the incompressible case. Alternatively, the pressure distribution could be matched, but matching $u_e(x)$ eases comparison with our incompressible vorticity-based code. The beginning of the PNS integration domain

is close to the leading edge, far upstream of the DNS domain start in order to keep influences from the inflow at a minimum where Blasius profiles are prescribed as an inflow boundary condition. At the upper boundary the streamwise pressure gradient has to be specified. The compressible Bernoulli equation along a streamline (subscript s) is considered:

$$\int \frac{\mathrm{d}\bar{p}}{\bar{\rho}} + \frac{\bar{q}^2}{2} = const. \tag{A 1}$$

When substituting $\bar{\rho}$ by $\bar{p}$ using the isentropic relations, (A 1) can be written as $\partial\bar{p}/\partial\bar{s} = f(\bar{u}, \partial\bar{u}/\partial\bar{s})$, which is known from the incompressible base flow. Dirichlet boundary conditions can then be prescribed for $\bar{T}_e(\bar{x})$ and $\bar{\rho}_e(\bar{x})$ using the isentropic relations. The non-dimensional $u_e(x)$ distribution can be matched perfectly to the incompressible one by this procedure.

The variables for the upstream boundary of the PNS domain at $\bar{x}_0 = 0.0034$ m depend on the initial choice of the Mach number based on the oncoming flow $\bar{q}_e(\bar{x}_0) = \{\bar{w}_e\,(\bar{x}_0)^2 + \bar{u}_e\,(\bar{x}_0)^2\}^{1/2}$, set to $Ma_q(\bar{x}_0) = \bar{q}_e(\bar{x}_0)/\bar{a}(\bar{x}_0) = 0.20$. The density is chosen to be $\bar{\rho}(\bar{x}_0) = 1.225$ kg m^{-3}. To match the kinematic viscosity of the incompressible case ($\bar{\nu} = 1.52 \times 10^{-5}$ m^2 s^{-1}), the temperature is set to $\bar{T}_e(\bar{x}_0) = \bar{T}_{wall} = 303.4$ K. We find $\bar{q}_e(\bar{x}_0) = 69.84$ m s^{-1}, and by varying the angle of the oncoming flow such that the incompressible streamwise velocity distribution $u_e(x)$ is met, yielding $\Phi(\bar{x}_0) = 72.58°$, the spanwise and streamwise velocity components are $\bar{w}_e(\bar{x}_0) = \bar{w}_e = 66.63$ m s^{-1} and $\bar{u}_e(\bar{x}_0) = 20.91$ m s^{-1}, respectively.

We prescribe free-stream boundary conditions $\bar{w}_e = const.$, $\bar{T}_e(\bar{x})$, $\bar{\rho}_e(\bar{x})$, $\partial\bar{p}/\partial\bar{x}(\bar{x})$, thus matching $u_e(x)$. For simplicity, Blasius inflow profiles were given, and hence the resulting cross-flow component $w_s(y)$ did not match the distribution obtained from the DLR experiment and the incompressible base flow. Therefore, we adapt the solution once at $\bar{x}_a = 0.0154$ m. Enlarging $w_s(x_a, y)$ gives modified u and w profiles that match the incompressible cross-flow development that in turn had also been matched (Bonfigli 2006) to the well-documented experimental development.

The second step, the steady Navier–Stokes solution, is carried out in two parts to obtain the final base flow. First, a preliminary DNS domain is used employing PNS velocity profiles at the inflow ($\bar{x}_{s1} = 0.0192$ m); see figure 15. Then the final DNS domain 2 is considered where profiles from the first DNS solution are used for the inflow boundary condition at $\bar{x}_{s2} = 0.0217$ m. Both domains end at $\bar{x}_{e12} = 0.1192$ m. For both DNS domains, PNS values are prescribed at the free-stream boundary.

Note that the final domain for the DNS base flow described here is larger than the domain used for the unsteady DNS, which covers $\bar{x} \in (0.0365\text{ m}, 0.0822\text{ m})$.

Similarly to the incompressible case, the reference velocity is chosen at a flow angle $\Phi_\infty = 42.5°$ and yields $\bar{U}_\infty = \bar{w}_{e,0}/\tan\phi_\infty = 72.72$ m s^{-1}. Defining $Re = 92\,000$ and keeping $\bar{\nu} = 1.52 \times 10^{-5}$ m^2 s^{-1}, the reference length is $\bar{L} = 0.01923$ m. Additionally, $\bar{T}_\infty = \bar{T}(\bar{x}_0)$ and $\bar{\rho}_\infty = \bar{\rho}(\bar{x}_0)$ are used for normalization.

Boundary-layer parameters for the converged base flow are compared with the incompressible ones in figure 16. Incompressible and compressible displacement and momentum thickness are obtained by integrating a pseudo-velocity distribution $u_p = \int_0^{y_e} \omega_z\,\mathrm{d}y$ to suppress influences from slightly non-constant $u(y)$ values at $x = const.$ outside the boundary layer. The wall-normal density variation is neglected in this calculation of the thickness. The Mach number $M_{s,e}$ based on $\bar{u}_{s,e}$ for the compressible case (not shown) varies between 0.229 and 0.264 in the compressible domain. The identical u_e development and the nearly constant Hartree parameters

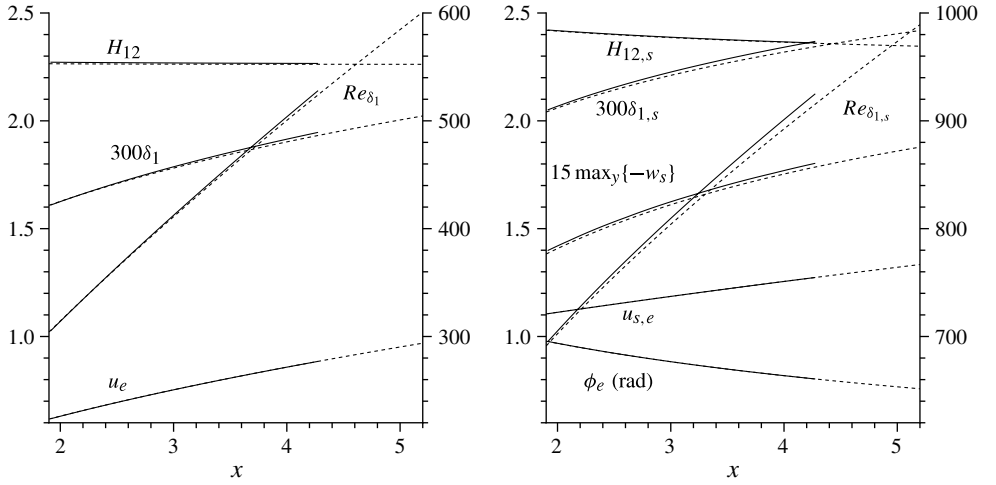

FIGURE 16. Boundary-layer parameters for incompressible base flow (dotted lines) and compressible base flow (solid lines). The compressible domain covers $x \in (1.9, 4.3)$. Right ordinates show Re_{δ_1} and $Re_{\delta_{1,s}}$. Values in the left plot are evaluated in the body-fixed coordinate system, in the right plot the streamline-oriented system is used. Note that to get the $\tilde{w}_s$ distribution w_s has to be divided by the local $u_{s,e}$ value.

Case	$d/\hat{d}$	$v_{max}/\hat{v}_{max}$	$(v_{max}/\hat{v}_{max})^2$	$\dot{m} \sim d^2 v_{max}$	$i \sim d^2 v_{max}^2$
A	1	1	1	1	1
B, C	$d/\hat{d}$	$(\hat{d}/d)^2$	$(\hat{d}/d)^4$	1	$(\hat{d}/d)^2$
B	0.75	1.78	3.16	1	1.78
C	0.6	2.78	7.72	1	2.78
B*	$d/\hat{d}$	$\hat{d}/d$	$(\hat{d}/d)^2$	$d/\hat{d}$	1
B*	0.75	1.33	1.78	0.75	1

$\hat{\boldsymbol{d}} = 20\,\Delta x$, $\hat{\boldsymbol{v}}_{max} = 0.200 u_\infty = 0.165 u_{s,e}$

TABLE 3. Mass and momentum fluxes for cases considered in appendix B.

indicate virtually identical flow fields. The slightly increased growth of the boundary-layer thickness arises from weak compressible effects. The somewhat higher values for the wall-normal velocity component seem to compensate for the decreasing density when proceeding downstream, as can be seen from figure 17, where velocity profiles are compared for the incompressible and compressible case. The location $x = 4.0$ has been chosen because the largest deviation is expected there. Also, density and temperature profiles of the compressible base flow are shown. Note that the magnitudes of ρ and T vary less than 2 % in the compressible solution.

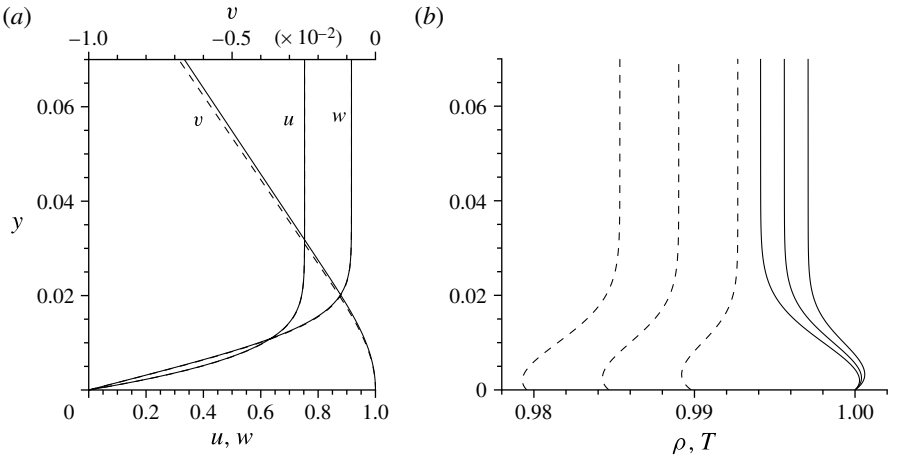

FIGURE 17. (*a*) Base-flow velocity profiles from the incompressible (dashed lines) and compressible (solid lines) case at $x = 4.0$. (*b*) Density (dashed lines) and temperature (solid lines) profiles at $x = 2.0,\ 3.0,\ 4.0$ (decreasing with increasing x).

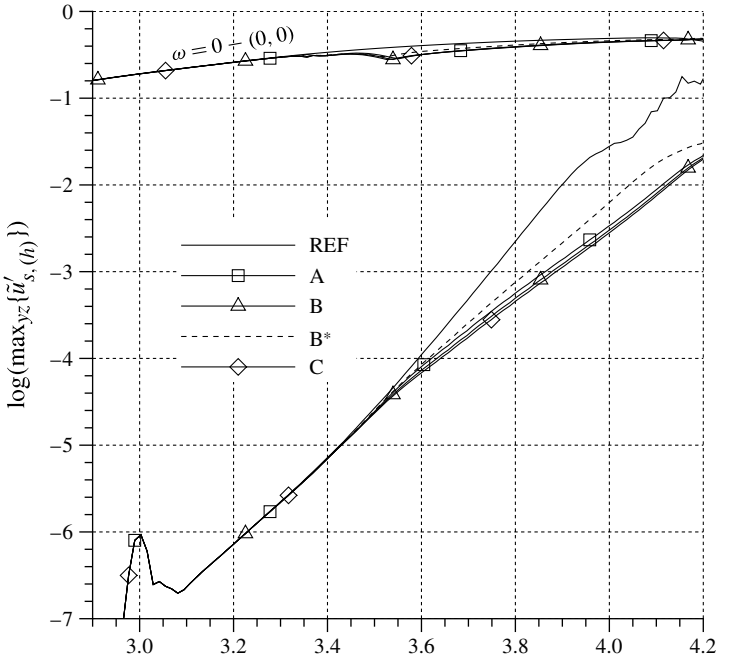

FIGURE 18. Downstream development of modal $\tilde{u}'_{s,(h)}$ amplitudes from Fourier analysis in time (maximum over y and z). Shown are the maximum steady three-dimensional deformation ($\omega = 0 - (0, 0)$) and one selected mode $\omega = 108$ for the reference case and three suction cases (see table 3).

A.3. *Numerical parameters for the compressible case*

The validation simulation results shown in figure 2 are obtained with the following parameters: the integration domains covers $1.900 \leqslant x \leqslant 4.276$ and $0.000 \leqslant y \leqslant 0.077$

and is resolved by approximately five million grid points, $N_x \times N_y \times N_z = 1816 \times 95 \times 32$, with $\Delta x = 1.309 \times 10^{-3}$, $\Delta y_{wall} = 2.300 \times 10^{-4}$ and $\Delta z = 3.747 \times 10^{-3}$ (corresponding to 10 spanwise Fourier modes). The fundamental spanwise wavenumber is $\gamma_0 = 52.4$ and the time step is $\Delta t = 1.047 \times 10^{-5}$. The parameters for the disturbance strips and the suction hole are identical to those described in table 2 for the incompressible case 1-H.

Appendix B. Effect of suction-hole diameter

We consider suction distributions according to (2.2) and calculate mass as well as momentum fluxes for cases with one suction hole per vortex and varying hole diameters (see table 3). Case A employs the suction hole with diameter $d = \hat{d}$ and maximum suction velocity $v_{max} = \hat{v}_{max} = 0.2u_\infty$. The suction holes in cases B and C provide the same mass fluxes with the hole diameters decreased by 25 and 40 %, respectively. For case B* the suction hole is 25 % smaller, set up such that the same momentum flux is obtained as in case A. Figure 18 shows the downstream modal development of selected $\tilde{u}'_s$ amplitudes. We observe an almost identical attenuation of secondary growth for cases A, B and C whereas case B* results in less attenuation. The effect of localized suction for the investigated hole set-ups depends on the mass flux sucked rather than on the momentum flux associated with it.

REFERENCES

BABUCKE, A., LINN, J., KLOKER, M. J. & RIST, U. 2006 Direct numerical simulation of shear flow phenomena on parallel vector computers. In *High Performance Computing on Vector Systems 2005* (ed. M. Resch *et al.*), *Proc. High Performance Computing Center Stuttgart (HLRS)*, pp. 229–247. Springer.

BIPPES, H. 1999 Basic experiments on transition in three-dimensional boundary layers dominated by cross-flow instability. *Prog. Aerosp. Sci.* **35**, 363–412.

BONFIGLI, G. 2006 Numerical simulation of transition and early turbulence in a 3-D boundary layer perturbed by superposed stationary and travelling cross-flow vortices. Dissertation, University of Stuttgart.

BONFIGLI, G. & KLOKER, M. J. 2007 Secondary instability of cross-flow vortices: validation of the stability theory by direct numerical simulation. *J. Fluid Mech.* **583**, 229–272.

FRIEDERICH, T. A. & KLOKER, M. J. 2008 Localized blowing and suction for direct control of the cross-flow secondary instability. *AIAA Paper* 2008-4394.

FRIEDERICH, T. A. & KLOKER, M. J. 2011 Control of crossflow-vortex induced transition: DNS of pinpoint suction. *AIAA Paper* 2011-3884.

JOSLIN, R. D. 1998*a* Overview of laminar flow control. NASA, TP-1998-208705. Langley Research Center, Hampton, VA.

JOSLIN, R. D. 1998*b* Aircraft laminar flow control. *Annu. Rev. Fluid Mech.* **30**, 1–29.

KLOKER, M. J. 2008 Advanced laminar flow control on a swept wing – useful cross-flow vortices and suction. *AIAA Paper* 2008-3835.

KOCH, W., BERTOLOTTI, F. P., STOLTE, A. & HEIN, S. 2000 Nonlinear equilibrium solutions in a three-dimensional boundary layer and their secondary instability. *J. Fluid Mech.* **406**, 131–174.

MALIK, M. R., LI, F., CHOUDHARI, M. M. & CHANG, C.-L. 1999 Secondary instability of cross-flow vortices and swept-wing boundary-layer transition. *J. Fluid Mech.* **399**, 85–115.

MESSING, R. & KLOKER, M. J. 2010 Investigation of suction for laminar flow control of three-dimensional boundary layers. *J. Fluid Mech.* **658**, 117–147.

SARIC, W. S., CARPENTER, A. L. & REED, H. L. 2008 Laminar flow control flight test for swept wings: strategies for LFC. *AIAA Paper* 2008-3834.

SARIC, W. S., CARRILLO, R. & REIBERT, M. 1998*a* Leading-edge roughness as a transition control mechanism. *AIAA Paper* 98-0781.

SARIC, W. S., CARRILLO, R. & REIBERT, M. 1998*b* Nonlinear stability and transition in 3-D boundary layers. *Meccanica* **33**, 469–487.

SARIC, W. S., REED, H. L. & WHITE, E. B. 2003 Stability and transition of three-dimensional boundary layers. *Annu. Rev. Fluid Mech.* **35**, 413–440.

SCHMIDT, O. T. & RIST, U. 2011 Linear stability of compressible flow in a streamwise corner. *J. Fluid Mech.* **688**, 569–590.

SCHRAUF, G. 2005 Status and perspectives of laminar flow. *Aeronaut. J.* **109** (1102), 639–644.

WASSERMANN, P. & KLOKER, M. J. 2002 Mechanisms and passive control of cross-flow-vortex induced transition in a three-dimensional boundary layer. *J. Fluid Mech.* **456**, 49–84.

WASSERMANN, P. & KLOKER, M. J. 2003 Transition mechanisms induced by travelling cross-flow vortices in a three-dimensional boundary layer. *J. Fluid Mech.* **483**, 67–89.

WASSERMANN, P. & KLOKER, M. J. 2005 Transition mechanisms in a three-dimensional boundary-layer flow with pressure-gradient changeover. *J. Fluid Mech.* **530**, 265–293.

WHITE, E. B. & SARIC, W. S. 2005 Secondary instability of cross-flow vortices. *J. Fluid Mech.* **525**, 275–308.